

Banner appropriate to article type will appear here in typeset article

Low-wavenumber wall pressure fluctuations in turbulent flows within concentric annular ducts

Yaomin Zhao^{1,2}, Taiyang Wang^{1,2} and Benshuai Lyu^{1†}

¹State Key Laboratory of Turbulence and Complex Systems, College of Engineering, Peking University, Beijing 100871, China.

²HEDPS, Center for Applied Physics and Technology, College of Engineering, Peking University, Beijing 100871, China.

(Received xx; revised xx; accepted xx)

Compressible direct numerical simulations of turbulent channel flows in concentric annular ducts of height 2δ are performed to study the low-wavenumber wall pressure fluctuations (WPF) over cylindrical walls at a bulk Mach number $M_b = 0.4$ and bulk Reynolds number $Re_b = 3000$. The radius of the inner cylinder R is varied between 0.2δ , δ , 2δ and ∞ . As R decreases, the one-point power spectral density of the WPF decreases at intermediate but increases at high frequencies. When R decreases, the 1D (streamwise) wavenumber-frequency spectrum of the WPF decreases at high wavenumbers. At low wavenumbers, however, as R reduces to 0.2δ the 1D wavenumber-frequency spectrum exhibits multiple spectral peaks whose strengths increase with frequency. Examination of the 2D wavenumber-frequency spectra shows that these represent acoustic duct modes that closely match theoretical predictions. The acoustic modes of higher radial orders exhibit increasingly high amplitude on the inner than on the outer walls. The low-wavenumber components of the 0th-order (azimuthal) 2D wavenumber-frequency spectrum are of great importance in practice, and their magnitude increases as R reduces; this increase is increasingly pronounced at higher frequencies. Analytical modelling and numerical validation show that this increase appears to arise from the “geometric” effects connected with the Green’s function, and they are generated mainly by radial and azimuthal disturbances. Disturbances closer to the wall are shown to be increasingly important in WPF generation as R reduces, which highlights a potential in WPF control using wall treatment on thin cylinders.

† Email address for correspondence: b.lyu@pku.edu.cn

Key words:

1. Introduction

Turbulent flows exert unsteady wall pressure loadings over solid walls. The wall pressure fluctuations (WPF) play an essential role in sonic loading in rocket sensor fairings, flow noise inside towed sonar arrays, and flow-induced vibration of pipelines. A clear characterisation and understanding of their statistics, spectra, and control are crucial in the aviation and ocean engineering industry ([Blake 1970](#)).

Extensive research has been conducted to characterise the WPF beneath turbulent boundary layers, with early research mainly on incompressible flows over flat plates. [Willmarth \(1956\)](#) appeared to be the first to measure basic statistics such as the root mean square (rms) value and frequency spectra of the WPF. Further experiments conducted by [Harrison \(1958\)](#) and [Willmarth \(1958\)](#) studied the WPF's space-time correlation and showed that the convection velocity was around 80% of the freestream velocity. [Bull \(1967\)](#), on the other hand, reported that the convection velocity depends on frequency. Regarding analytical models, [Kraichnan \(1956\)](#) was among the first to develop a mirror-flow model and showed that the rms value of the WPF was roughly six times the mean wall shear stress, a result that agreed well with the measured values by [Willmarth \(1956\)](#) and many others ([Bull 1996](#)). Based on streamwise and lateral correlation similarity, [Corcos \(1963\)](#) proposed a model for the cross-spectral density of the WPF, applicable to the wavenumber regime near ω/U_c , where ω and U_c represent the angular frequency and convection velocity of the WPF, respectively. Comprehensive reviews of these early studies can be found in [Willmarth \(1975\)](#) and [Bull \(1996\)](#).

However, realistic applications often involve wall surfaces with curvature, such as the hose of a towed sonar array. Incompressible WPF over curved surfaces was studied subsequently. This includes, for example, early experiments by [Willmarth & Yang \(1970\)](#) and [Willmarth *et al.* \(1976\)](#). They concluded that the wall curvature caused insignificant changes in the frequency spectra and convection velocity but a noticeable reduction in the spanwise correlation length. Analytical modelling was conducted by [Howe \(1987\)](#) and [Dowling \(1998\)](#), the latter of which modelled the incompressible wavenumber-frequency spectrum using Lighthill's acoustic analogy. The effect of wall curvature on WPF was also examined using direct numerical simulations (DNS), where [Neves & Moin \(1994b\)](#) showed that increasing curvature reduced both spatial and temporal spectra of the WPF at all scales, decreased the azimuthal correlation length, increased the streamwise correlation length, and reduced the convection velocity. Note that the curvature examined in their studies

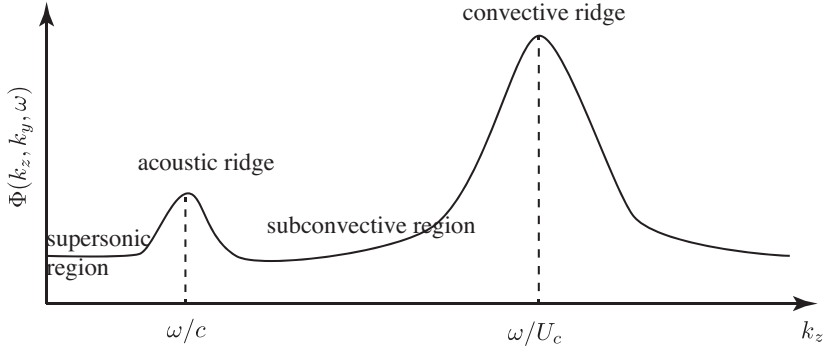


Figure 1: A typical wavenumber-frequency spectrum of the WPF at a given frequency ω and spanwise wavenumber $k_y = 0$. k_z represents the streamwise wavenumber.

was substantially larger than that in [Willmarth & Yang \(1970\)](#) and [Willmarth *et al.* \(1976\)](#).

A typical wavenumber-frequency spectrum at a given frequency ω is shown in figure 1. A high-wavenumber peak called convective ridge is located at $k_z = \omega/U_c$ due to turbulence convection, where k_z represents the streamwise wavenumber. In contrast, a low-wavenumber acoustic ridge appears at $k_z = \omega/c_0$, where c_0 is the speed of sound. Note that, however, it is the low-wavenumber components of the WPF, i.e., the subconvective and supersonic regions shown in figure 1, that are of particular interest in practice. This is because they are more likely to couple with the elastic motion of the solid walls or are responsible for direct acoustic radiation. In such regimes, compressibility is crucial, even in very low Mach number flows; it is therefore essential to include the effects of compressibility in the study of WPF. For example, using Lighthill's acoustic analogy, [Ffowcs-Williams \(1965\)](#) showed that including compressibility resulted in the violation of the Kraichnan-Phillips theorem and led to a non-zero spectral magnitude proportional to the square of the mean-flow Mach number at zero wavenumbers.

The magnitude of the wavenumber-frequency spectrum around the acoustic ridge, as can be seen from figure 1, is often much lower than that near the convective ridge. This poses significant challenges to resolving the low-wavenumber components using either experiments or numerical simulations. As such, compressible simulations that study the subconvective and supersonic regions remain scarce. [Gloerfelt & Berland \(2013\)](#) and [Cohen & Gloerfelt \(2018\)](#) were among the first to study the acoustic component of the WPF beneath a turbulent boundary layer of Mach 0.5 using large eddy simulations (LES). They were able to capture the acoustic ridge, but were unable to fully eliminate errors caused by artificial boundaries. A recent study by [Liu *et al.* \(2024\)](#) showed that with suitable choices of low-dissipative and low-dispersive schemes, it is possible to accurately resolve these low-energy components

Case	Re_b	Re_τ (inner, outer)	ϵ	L_θ, L_r, L_z	N_θ, N_r, N_z	Δ_θ^+	Δ_r^+	Δ_z^+
1	3000	188	∞	$\frac{4}{3}\pi\delta, 2\delta, 16\pi\delta$	256, 193, 1024	3.08	0.20 – 2.40	9.23
2	3000	193, 183	2	$4\pi\delta, 2\delta, 16\pi\delta$	800, 193, 1024	3.11 – 6.23	0.43 – 5.8	9.73
3	3000	198, 183	1	$2\pi\delta, 2\delta, 16\pi\delta$	400, 193, 1024	3.20 – 9.59	0.25 – 6.71	9.99
4	3000	230, 182	0.2	$\frac{2}{5}\pi\delta, 2\delta, 16\pi\delta$	300, 193, 1024	0.99 – 10.87	0.56 – 6.71	11.58

Table 1: Simulation matrix and parameters used in each simulation. N_i and Δ_i^+ represent the number and non-dimensional of the grid element in i direction ($i = \theta, r$ and z).

using compressible DNS. The DNS was performed on a rectangular channel with periodic boundary conditions to suppress the artefacts introduced by the boundary conditions.

However, as mentioned above, practical applications are rarely characterised by flat plates, but rather by surfaces with curvature. To the best of the authors' knowledge, compressible flow simulations focusing on the low-wavenumber region of the WPF over surfaces with curvature remain to be seen. The characteristics of the low-wavenumber components of the WPF over cylindrical walls, in particular, how energetic they are compared to convective components as the curvature varies, remain largely unknown. In this paper, we aim to bridge the gap and study the wall pressure over cylindrical surfaces of various curvatures. To directly resolve these low-frequency components, we resort to DNS with low-dissipative and low-dispersive finite-difference schemes. Similar to [Liu et al. \(2024\)](#), to avoid the inevitable noise introduced by artificial boundary conditions, channel flows within a concentric annular duct are simulated with a periodic boundary condition in the streamwise direction. In doing so, not all the features of the free boundary layer can be captured, but the important effects of curvature are kept without complications introduced by simulating free boundary layers ([Neves & Moin 1994b](#)).

This paper is structured as follows. Section 2 introduces the computational setup and discretisation schemes used in this study. Section 3 validates the simulations and discusses the effects of curvature on flow statistics. Section 4 shows the power spectral density (PSD) and wavenumber-frequency spectra of the WPF over cylinders of various diameters. Section 5 uses Lighthill's acoustic analogy to model the WPF generated by cylindrical boundary layers, with which the mechanisms of the low-wavenumber WPF augmentation are discussed. The following section concludes the paper and lists future work.

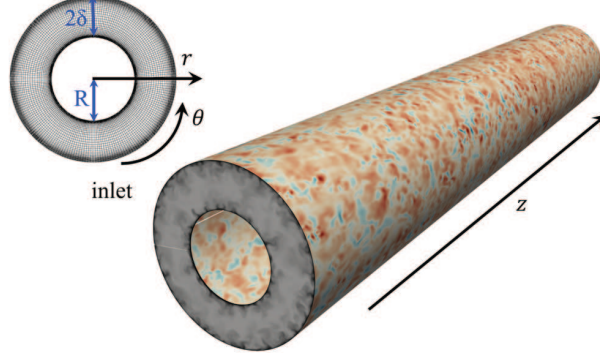


Figure 2: DNS configurations, with θ , r , and z denoting the circumferential, radial, and axial directions, respectively. The contours of instantaneous velocity magnitude and pressure are shown on the inlet and inner and outer walls, respectively.

2. Numerical setup

A schematic setup of the simulations is shown in figure 2. The channel flow within an annular duct is discretised on a generalised curvilinear coordinate system, with θ , r and z denoting the azimuthal, radial, and axial directions, respectively. L_r and L_z represent the channel height and length, while R and L_θ denote the radius and the circumference of the inner cylindrical wall, respectively. In the θ and z directions, grid points are uniformly distributed, with periodic conditions applied at the boundaries. A no-slip isothermal condition is imposed on the walls, and the grid near the wall is refined based on a hyperbolic tangent function. The parameters of all four DNS simulations are listed in Tab. 1, where ϵ is defined as R/δ to represent the non-dimensional radius of the inner cylinder. Case 1 is a plane channel for comparison, where L_θ reduces to the spanwise domain size. Note that the channel length L_z is deliberately chosen to be $16\pi\delta$ in order to resolve the low-wavenumber components of the WPF.

The code HiPSTAR (Sandberg *et al.* 2015), which has been extensively validated for acoustic simulations (Deuse & Sandberg 2020), is used to solve the non-dimensionalized three-dimensional (3D) compressible Navier-Stokes equations

$$\frac{\partial \rho}{\partial t} + \frac{\partial(\rho u_j)}{\partial x_j} = 0, \quad (2.1a)$$

$$\frac{\partial(\rho u_i)}{\partial t} + \frac{\partial(\rho u_i u_j + p \delta_{ij})}{\partial x_j} = \frac{\partial \tau_{ij}}{\partial x_j}, \quad (2.1b)$$

$$\frac{\partial(\rho e_0)}{\partial t} + \frac{\partial[u_j(\rho e_0 + p)]}{\partial x_j} = \frac{\partial(\tau_{ij} u_i)}{\partial x_j} - \frac{\partial q_j}{\partial x_j}. \quad (2.1c)$$

Here, ρ , u_i , p and T denote the non-dimensionalised flow density, velocity components, pressure and temperature, respectively.

The non-dimensionalization results in dimensionless parameters as $Re_b = (\rho_b U_b \delta) / \mu_\infty = 3000$ and $M_b = U_b / c_\infty = 0.4$, where δ , U_b and ρ_b are the channel half-height, mean bulk velocity and density, respectively. Moreover, μ_∞ and c_∞ are viscosity and acoustic velocity for the reference state which are only dependent on the reference wall temperature T_w . The total energy e_0 is given by

$$e_0 = \frac{\rho u_i u_i}{2} + \frac{1}{\gamma(\gamma - 1) M_b^2} T, \quad (2.1)$$

where $\gamma = 1.4$ is the specific heat ratio. Moreover, the stress tensor is written as

$$\tau_{ij} = \frac{\mu}{Re_b} \left(\frac{\partial u_i}{\partial x_j} + \frac{\partial u_j}{\partial x_i} - \frac{2}{3} \frac{\partial u_k}{\partial x_k} \delta_{ij} \right), \quad (2.2)$$

and the molecular viscosity μ is computed using Sutherland's law (([White 1991](#))). Similarly, the heat flux q_j is written as

$$q_j = -\frac{\mu}{(\gamma - 1) Pr Re_b M_b^2} \frac{\partial T}{\partial x_j}, \quad (2.3)$$

where Pr is the Prandtl number and takes the value of 0.72.

A fourth-order finite difference scheme was applied for spatial discretisation, while the ultra-low storage frequency optimised explicit Runge-Kutta method ([Kennedy et al. 2000](#)) was used for time integration. In addition, the non-linear terms are processed with a skew-symmetric splitting method ([Kennedy & Gruber 2008](#)) to reduce aliasing, and a standard filtering scheme ([Bogey & Bailly 2004](#)) is used to improve numerical stability. Simulations are conducted for around 48 flow-through time units on GPUs, after which the wall pressure on the inner cylinder surface and velocity data within the channel are stored for analysis. Detailed sampling frequency and sampling duration are shown in section 4.

3. Validation and flow statistics

Before examining the WPF, we first validate the present DNS by comparing the flow statistics against those in the literature. The effects of curvature on the flow statistics are shown subsequently. To facilitate an examination of the turbulent statistics distribution along the wall-normal direction, a radial distance measured from the inner cylinder wall, defined as $y = r - R$, is used. This distance is often presented in wall units defined by $y^+ = y u_\tau / \nu$, where ν and u_τ represent the kinematic viscosity and wall friction velocity of the flow, respectively.

3.1. Validation of the DNS

To validate the present simulations, the mean and fluctuation velocities are first compared against results published previously. Note that the fluctuation velocities

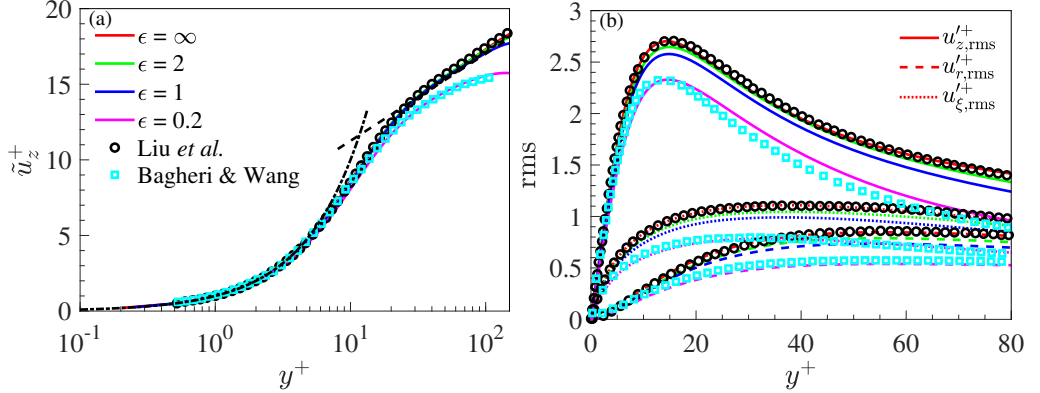


Figure 3: Comparison of (a) mean velocity profiles and (b) rms of velocity fluctuations between the present cases and previous simulations. Circle, plane channel case in [Liu et al. \(2024\)](#); square, case with $\epsilon = 0.22$ in [Bagheri & Wang \(2020\)](#).

are defined by removing the mean values defined by the Favre average ($\tilde{\cdot}$), i.e.

$$\tilde{u}_i = \langle \rho u_i \rangle / \langle \rho \rangle, \quad (3.0a)$$

$$u'_i = u_i - \tilde{u}_i, \quad (3.0b)$$

where $\langle \cdot \rangle$ represents ensemble average. In practice, temporal and spatial (streamwise and azimuthal) averages are used instead. It is worth noting that although the bulk Mach number M_b is 0.4, the density variation of the flow is very limited. As such, the difference between the direct and Favre averages is negligible. The mean and fluctuation velocities are subsequently normalised by the friction velocity u_τ to obtain \tilde{u}_i^+ and u'_i^+ , respectively.

The comparison of the two velocities is shown in figure 3, among which figure 3(a) shows the distribution of the axial mean velocity along the wall-normal direction. In the rectangular case, the viscous sublayer and log law of the wall are captured and compared well to [Liu et al. \(2024\)](#). When the radius of the inner cylinder reduces to $\epsilon = 2$ or 1, the velocity distribution shows minimal change, in contrast to the significant changes at $\epsilon = 0.2$. In particular, the axial mean velocity decreases in the outer layer. The obtained velocity profile agrees well with [Bagheri & Wang \(2020\)](#), albeit the slight mismatches in the inner cylinder radius.

Figure 3(b) shows the rms value of the velocity fluctuations in the axial, radial, and azimuthal directions, respectively. In the rectangular case, we see that the velocity fluctuations compare very well with [Liu et al. \(2024\)](#). When the inner radius decreases, the velocity fluctuations continuously decrease, particularly in the outer layer of the flow. Note that the study of [Bagheri & Wang \(2020\)](#) was conducted for a $\epsilon = 0.22$, hence it is different from the present case of $\epsilon = 0.2$. This partly explains why there are slight mismatches in the rms values of the two cases. In addition, the

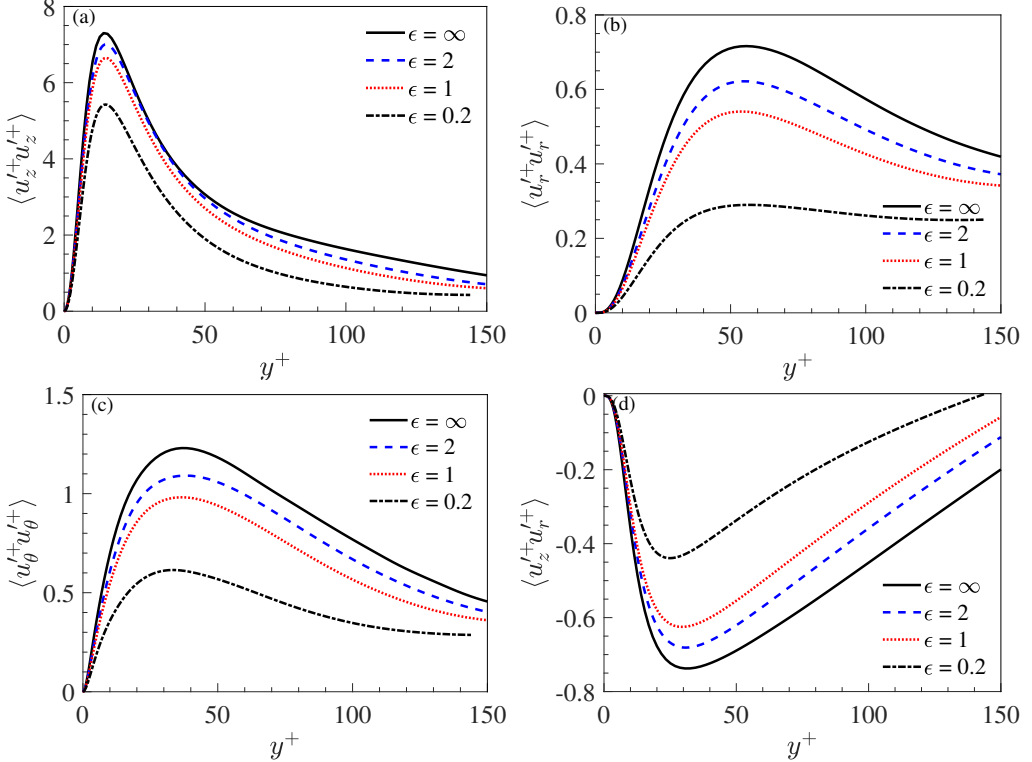


Figure 4: Wall normal distribution of the Reynolds stresses of (a) $\langle u_z'^2 \rangle$, (b) $\langle u_r'^2 \rangle$, (c) $\langle u_\theta'^2 \rangle$ and (d) $\langle u_z' u_r' \rangle$ over inner cylinder wall.

difference in the Mach number might also play a role as incompressible simulations were conducted in [Bagheri & Wang \(2020\)](#). Nevertheless, figure 3(b) still shows a relatively good agreement between the two cases. In light of the good agreement shown in figure 3, one expects that the current simulation captures the essential physics of turbulent channel flows within concentric annular ducts.

3.2. Effects of curvature on the flow field

To examine the effects of curvature on the flow closely, we show the distribution of the Reynolds stresses along the wall normal direction for various cylinder diameters. These are shown in figure 4. Figure 4(a) shows the wall-normal distribution of $\langle u_z'^2 \rangle$. One sees that this Reynolds stress component peaks at around $y^+ = 15$, while increasing the curvature appears to move this location slightly closer to the wall. This finding is consistent with the incompressible simulation by [Neves & Moin \(1994a\)](#). As the curvature increases from $\epsilon = \infty$ to $\epsilon = 1$, the amplitude of this component decreases slightly. As the curvature increases to $\epsilon = 0.2$ significant reduction occurs. This suggests that axial velocity fluctuations tend to be suppressed within boundary layers over thinner cylinders.

Figure 4(b) shows the wall-normal distribution of $\langle u_r'^2 \rangle$. A striking difference

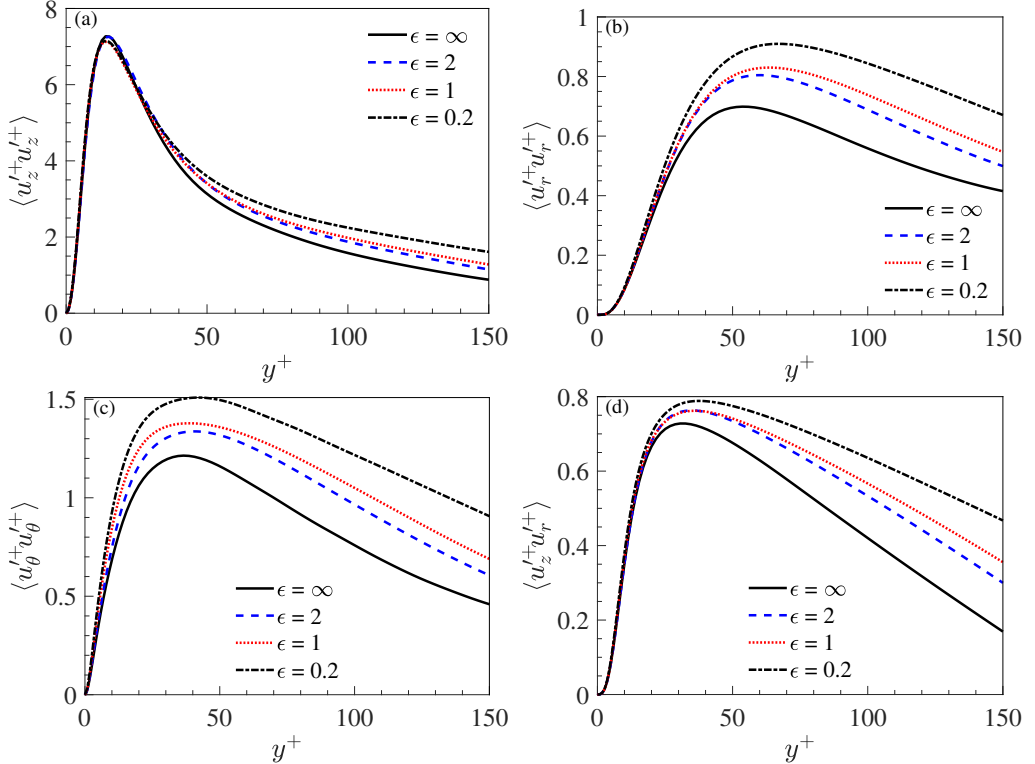


Figure 5: Wall normal distribution of the Reynolds stresses of (a) $\langle u_z' u_z' \rangle$, (b) $\langle u_r' u_r' \rangle$, (c) $\langle u_\theta' u_\theta' \rangle$ and (d) $\langle u_z' u_r' \rangle$ over outer cylinder wall.

is the amplitude that is an order of magnitude lower compared to that of $\langle u_z' u_z' \rangle$. This is well-known, implying that turbulent energy is dominated by the streamwise velocity fluctuations. In addition, this component peaks further away from the wall at $y^+ = 50$. Increasing curvature appears to shift this peak location slightly closer to the wall, but reduces the amplitude considerably. Such a decrease is evident even when $\epsilon = 2$ and $\epsilon = 1$. In particular, when $\epsilon = 0.2$, the profile shows a rather flat behaviour beyond $y^+ = 50$. Figure 4(c) shows the wall-normal distribution of $\langle u_\theta' u_\theta' \rangle$. The distribution of this component is very similar to that of $\langle u_r' u_r' \rangle$, apart from the fact that $\langle u_\theta' u_\theta' \rangle$ obtains slightly larger values. This shows that the azimuthal fluctuations are stronger than the radial fluctuations, a fact that does not appear to change with curvature.

Figure 4(d) shows the wall-normal distribution of $\langle u_z' u_r' \rangle$. Within the y^+ range shown in this figure, $\langle u_z' u_r' \rangle$ is negative, indicating that this is turbulent production term (Pope 2000). This component peaks around $y^+ = 25$. As the curvature increases, its magnitude decreases considerably. Since the flow field is statistically homogeneous along the z and θ directions, the Reynolds stresses $\langle u_z' u_\theta' \rangle$ and

$\langle u'_r u'_\theta \rangle$ are, as expected, approximately equal to 0. We omit their presentation in the text and only show them in Appendix A for reference.

Although we are interested in the WPF over the inner cylinder wall, it is interesting to examine how the curvature changes the flow over the outer cylinder wall. The curvature may be regarded as negative in this case. The Reynolds stresses are shown in figure 5. One can see that the effects of negative curvature on the flow are opposite to those of positive curvature for all the Reynolds stress components, i.e. they increase as the curvature increases. In addition, for all the stress components, their peak positions move slightly away from the wall, as opposed to moving closer to the wall for inner cylinders. Note that in figure 5(d), the $\langle u'_r u'_z \rangle$ obtain positive values. This is because the u'_r represents the negative wall-normal velocity component for the outer wall. As such, it still represents a term for turbulence production. The $\langle u'_z u'_\theta \rangle$ and $\langle u'_r u'_\theta \rangle$ are again close to 0, details of which are also shown in appendix A.

4. Results

Having validated the present DNS and discussed the effects of curvature on the velocity statistics, we are now in a position to examine how the curvature changes the characteristics of WPF. Note that the WPF $p'(z, \theta, t)$ is sampled with a time step $\Delta t U_b / \delta \approx 0.048$ for a total of around 8000 snapshots. The snapshot sequence is divided into a number of segments with a 50% overlap. This results in 20 segments, and each segment contains 768 snapshots and is Fourier transformed/expanded along z , θ and t to yield its spectrum $\tilde{p}(k_z, m, \omega)$, i.e.

$$\tilde{p}(k_z, m, \omega) = \int_0^T \int_0^{2\pi} \int_0^{L_z} p'(z, \theta, t) e^{-i\omega t} e^{ik_z z} e^{im\theta} dz d\theta dt. \quad (4.1)$$

This yields a resolved non-dimensional frequency up to $\bar{\omega} \equiv \omega \delta / U_b \approx 65$ with a resolution of around 0.165 and a resolved non-dimensional wavenumber up to $k_z \delta \approx 64$ with a resolution of around 0.125.

The two-dimensional (2D) wavenumber-frequency spectrum is obtained from

$$\Phi(k_z, m, \omega) = \frac{1}{(2\pi)^2 L_z T} \langle \tilde{p}(k_z, m, \omega) \tilde{p}^*(k_z, m, \omega) \rangle, \quad (4.2)$$

where T represents the temporal duration of each segment. Note that each segment is weighted by a Hanning window before the Fourier transform with respect to t is performed. This procedure is pivotal to revealing the low-wavenumber components simultaneously with the much more energetic convective ridge by suppressing spectral leaks.

The one-dimensional (1D) wavenumber-frequency spectrum is calculated by sum-

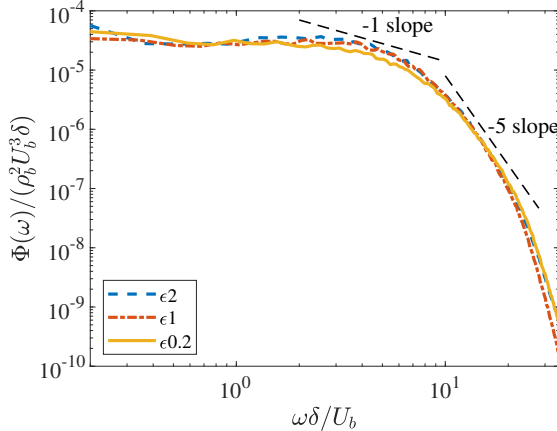


Figure 6: Nondimensionalized PSD $\Phi(\omega)/(\rho_b^2 U_b^3 \delta)$ of the WPF over cylinders of various diameters.

ming all azimuthal modes to yield

$$\Phi(k_z, \omega) = \sum_{m=-\infty}^{\infty} \Phi(k_z, m, \omega). \quad (4.3)$$

Similarly, the PSD of the WPF is obtained by

$$\Phi(\omega) = \frac{1}{2\pi} \int_{-\infty}^{\infty} \Phi(k_z, \omega) \, dk_z. \quad (4.4)$$

In the rest of this section, the PSD, 1D and 2D wavenumber-frequency spectra at different ϵ values are examined sequentially. Note that the spectra at $\epsilon = 2$ show minimal difference from those at $\epsilon = \infty$; hence, the $\epsilon = \infty$ case is omitted in the following comparison for conciseness and consistent definition of azimuthal modes (the $\epsilon = \infty$ case needs a different definition for azimuthal modes).

4.1. Power spectral density

Figure 6 shows the comparison of the one-point temporal spectra of the WPF over cylinders of various diameters. All spectra exhibit a ω^{-1} scaling in the intermediate but a ω^{-5} scaling in the high frequency regimes. This is similar to the plane channel flows (Liu *et al.* 2024; Bull 1996). Clearly, the spectra of $\epsilon = 2$ and $\epsilon = 1$ show minimal difference. This is well-known in incompressible studies - when the inner cylinder is large, the effects of curvature on the WPF are negligible (Neves & Moin 1994b). However, when ϵ reduces to 0.2, the wall pressure spectrum shows a clear reduction in magnitude in the intermediate frequency regime. At high frequencies, however, the spectral magnitude exhibits a slight increase compared to that at $\epsilon = 1$. The effects of curvature on the low-frequency PSD component appear rather limited. Note, however, this does not contradict the findings of Neves & Moin (1994b), where the PSD reduces at all frequencies when the friction velocity u_τ is used for non-

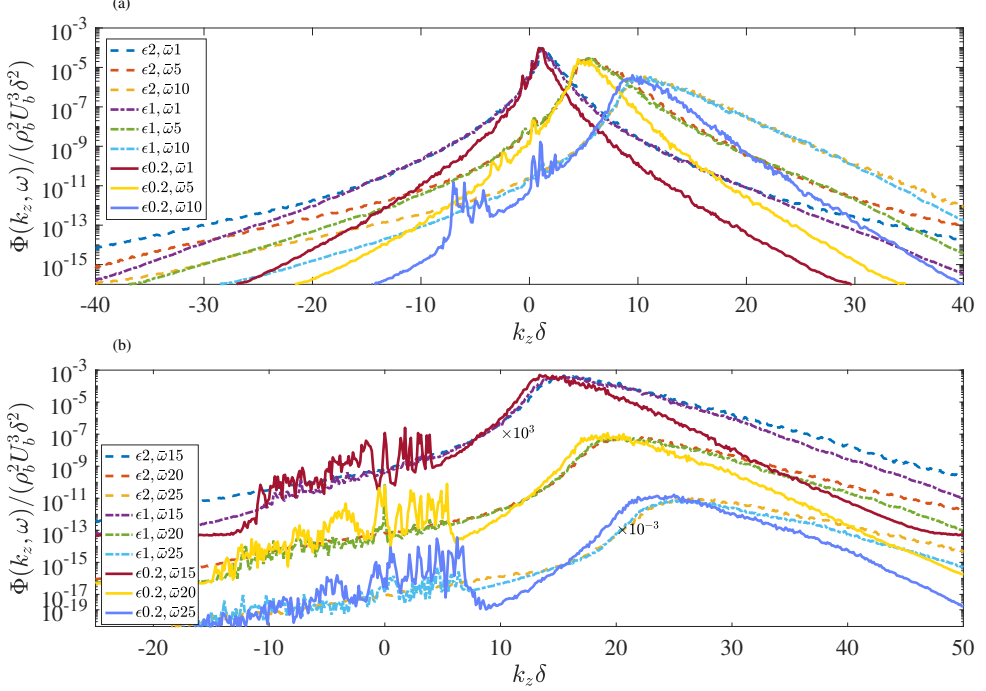


Figure 7: 1D wavenumber-frequency $\Phi(k_z, \omega) / (\rho_b^2 U_b^3 \delta^2)$ spectra of WPF for various cylinder diameters: (a) $\bar{\omega} = 1, 5$ and 10 ; (b) $\bar{\omega} = 15, 20$ and 25 the spectral magnitudes at $\bar{\omega} = 15$ and $\bar{\omega} = 25$ are multiplied by 10^3 and 10^{-3} respectively for separation clarity.

dimensionalisation. To examine the structures of the WPF, however, one is more interested in the wavenumber-frequency spectra shown in the following sections.

4.2. 1D wavenumber-frequency spectra

Figure 7(b-c) compares the 1D wavenumber-frequency spectra $\Phi(k_z, \omega)$ when ϵ varies. At a low frequency of $\bar{\omega} = 1$, one can see a clear dominant peak at the convective wavenumbers ω/U_c . Reducing the radius from $\epsilon = 2$ to 1 lowers the magnitude at high (including negative) wavenumbers. Further decreasing the cylinder radius to $\epsilon = 0.2$ reduces the spectra more significantly. However, the magnitude at the convective wavenumber appears virtually unchanged. This implies that the streamwise length scale of the WPF becomes larger, a result in accordance with earlier incompressible studies (Neves & Moin 1994b). In addition, one starts to see a significant spectral feature change when ϵ reduces to 0.2 , i.e. acoustic peaks (see section 4.3) start to appear in the supersonic wavenumber region.

As the frequency increases to $\bar{\omega} = 5$ and 10 , the convection peak moves to higher wavenumbers with reduced magnitudes, consistent with a decaying magnitude against frequency shown in figure 7(a). The effects of reducing ϵ are similar to those at $\bar{\omega} = 1$, except that the acoustic peaks at $\epsilon = 0.2$ are increasingly strong as the

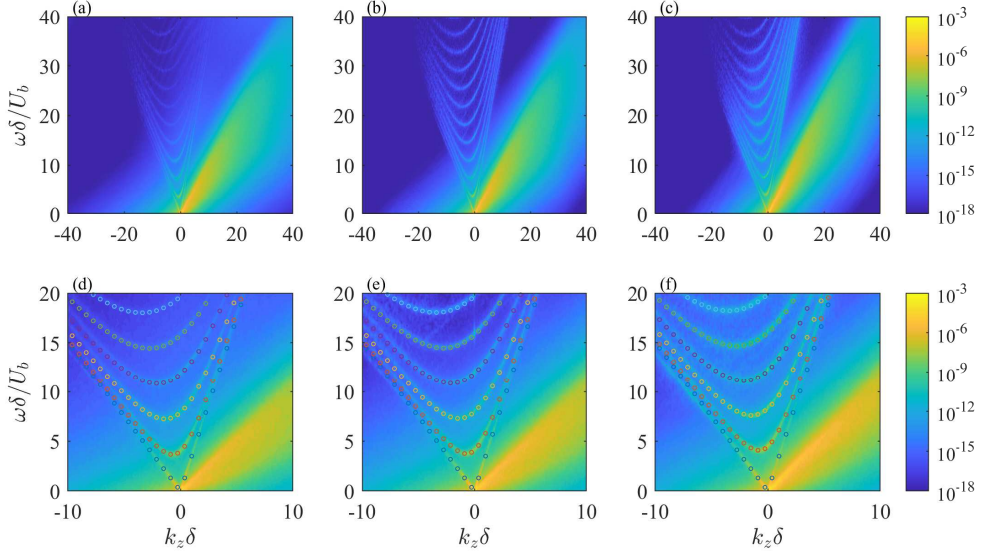


Figure 8: The 2D wavenumber-frequency spectra at $\epsilon = 2$ (a,d), 1 (b,c) and 0.2 (e,f). The dotted lines represent the acoustic duct modes solved from (4.5).

frequency increases. In addition, the spectra appear to shift to lower wavenumbers as R reduces.

The acoustic peaks and spectral shift are more significant at higher frequencies. Figure 7(c) shows the spectra at $\bar{\omega} = 15, 20$ and 25 , respectively. At $\bar{\omega} = 15$, the spectrum is smooth at all wavenumbers at $\epsilon = 2$ but starts to show some acoustic peaks at $\epsilon = 1$. At $\epsilon = 0.2$, a much denser cluster of acoustic peaks starts to occur. As the frequency increases to $\bar{\omega} = 20$ and 25 , these acoustic peaks are both stronger and denser. Note that acoustic peaks do not appear in the case of rectangular channels (Liu *et al.* 2024) and are caused by the curvature of the walls. Similar to the appearance of the acoustic peaks, the tendency of spectral shift appears increasingly evident as the frequency increases.

4.3. 2D wavenumber-frequency spectra

The fact that the spectral peaks observed in figure 7(c) are acoustics induced can be clearly seen from the 2D wavenumber-frequency spectra $\Phi(k_z, m, \omega)$. Considering that it is the axisymmetric mode ($m = 0$) that is more likely to couple with the elastic structures, figure 8 first shows the contour of $\Phi(k_z, 0, \omega)$ over cylinders of various diameters. Note that the colour is plotted in a logarithmic scale due to the wide span of the spectral magnitude.

Figure 8(a) shows $\Phi(k_z, 0, \omega)$ for $\epsilon = 2$. Due to compressibility, we see an evident violation of the Kraichnan-Phillips theorem that demands $\Phi(k_z, k_y, \omega) \rightarrow 0$ as $k_z^2 + k_y^2 \rightarrow 0$ (Ffowcs-Williams 1965), where k_y represents the spanwise wavenumber. Similar to the incompressible case (Neves & Moin 1994b), the energy of the WPF is

dominated by the convective ridges. As the frequency increases, however, these ridges become increasingly wide, suggesting a less well-defined convection velocity. What sets the compressible spectra apart from their incompressible counterparts, however, are a series of discrete curves clearly visible albeit at a much weaker intensity. These are the acoustic modes in annular ducts, which are similar to those in plane channel flows (Liu *et al.* 2024).

To examine these acoustic modes closely, figure 8(d-f) shows a close-up view of the low-wavenumber regimes of figure 8(a-c). Also included are the analytical dispersion relations of the acoustic modes in annular ducts with uniform mean flow (Crighton *et al.* 1992), i.e.

$$(\beta^2 k_z + k M_b)^2 = k^2 - \mu_{mn}^2 \beta^2, \quad (4.5)$$

where $\beta^2 = 1 - M_b^2$, $k = \omega/c_0$, while μ_{mn} is the n th root of

$$J'_m(\mu_{mn}R)Y'_m(\mu_{mn}(R + 2\delta)) - J'_m(\mu_{mn}(R + 2\delta))Y'_m(\mu_{mn}R) = 0. \quad (4.6)$$

In (4.6), J_m and Y_m represent the m th-order Bessel functions of the first and second kinds, respectively, the prime superscript represents their first derivatives, while n denotes an integer representing the radial order of the acoustic mode. One can see the nearly perfect collapse of these predicted duct modes with those discrete curves in figure 8(d-f). Note the striking difference in the spectral magnitudes of these acoustic modes and the convective ridge. However, as ϵ reduces, these acoustic modes appear to intensify, as shown by the increasingly bright lines in figure 8(b-f).

To examine the acoustic modes in detail, we plot their pressure distribution within the annular ducts of various diameters. These acoustic modes can be calculated analytically, and they take the form of

$$p = C_{mn} (Y'_m(\mu_{mn}R)J_m(\mu_{mn}r) - J'_m(\mu_{mn}R)Y_m(\mu_{mn}r)) \exp(im\theta) \exp(-ik_z z), \quad (4.7)$$

where, C_{mn} represents the normalisation constant that depends on the azimuthal order m and radial order n . In this paper, we focus on the axisymmetric mode $m = 0$ and use (4.7) to plot the acoustic mode propagating toward the $+z$ direction. Those propagating towards the $-z$ direction are similar and hence omitted.

The cross-sections of the duct modes for the three cylinder diameters are shown in figures 9 and 10 at a reduced frequency of $k\delta = 2$ and 5, respectively. Figure 9(a-c) shows the real part of (4.7) for the acoustic mode of radial order $n = 1$ at $k\delta = 2$. These represent plane wave modes (the straight discrete lines in figure 8) propagating along the $+z$ direction. In figure 8, we show that these plane-wave modes appear stronger on the inner cylinder wall as ϵ reduces. Since their amplitudes on the inner and outer cylinder walls remains identical, as shown in figure 9(a-c), one expects a similar behaviour on the outer wall.

Figure 9(d-f), on the other hand, shows the acoustic modes of the radial order

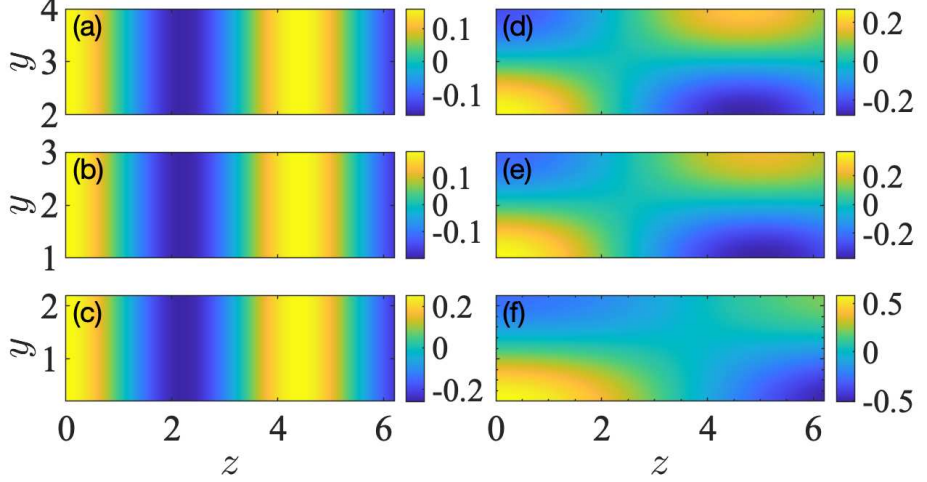


Figure 9: Axisymmetric ($m = 0$) acoustic modes at $k = 2$: (a-c) modes of radial order $n = 1$ (plane waves); (d-f) modes of radial order $n = 2$; (a,d): $\epsilon = 2$; (b,e) $\epsilon = 1$; (c, f) $\epsilon = 0.2$.

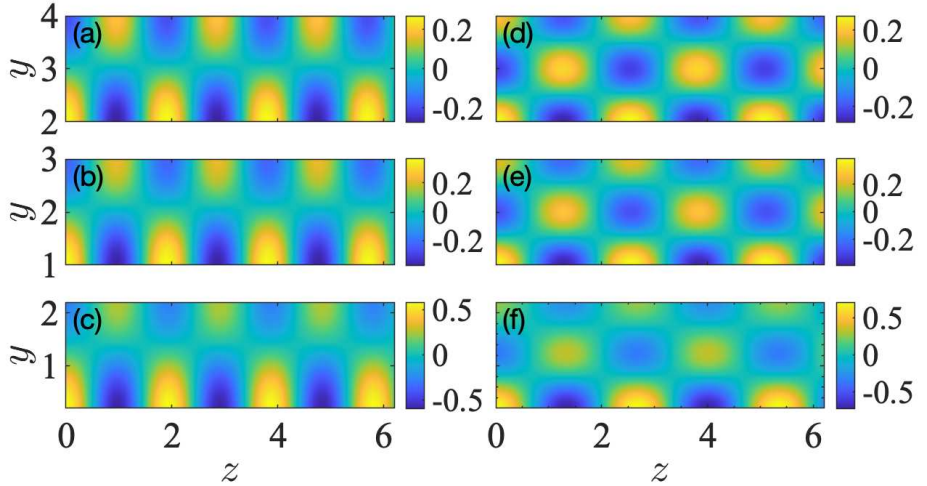


Figure 10: Axisymmetric ($m = 0$) acoustic modes at $k = 5$: (a-c) modes of radial order $n = 2$; (d-f) modes of radial order $n = 3$; (a,d): $\epsilon = 2$; (b,e) $\epsilon = 1$; (c, f) $\epsilon = 0.2$.

$n = 2$. It is worth noting that only two radial orders (1 and 2) are cut-on at this reduced frequency of $k\delta = 2$, while higher-order modes are effectively cut-off. This can be seen clearly from figure 8(d-f) by drawing a horizontal line at $\omega\delta/U_b = 5$. From figure 9(d-f), we can see that as the curvature increases, the acoustic pressure on the inner cylinder wall becomes increasingly larger than that on the outer wall. To put this difference into perspective, the acoustic pressure at the inner wall is

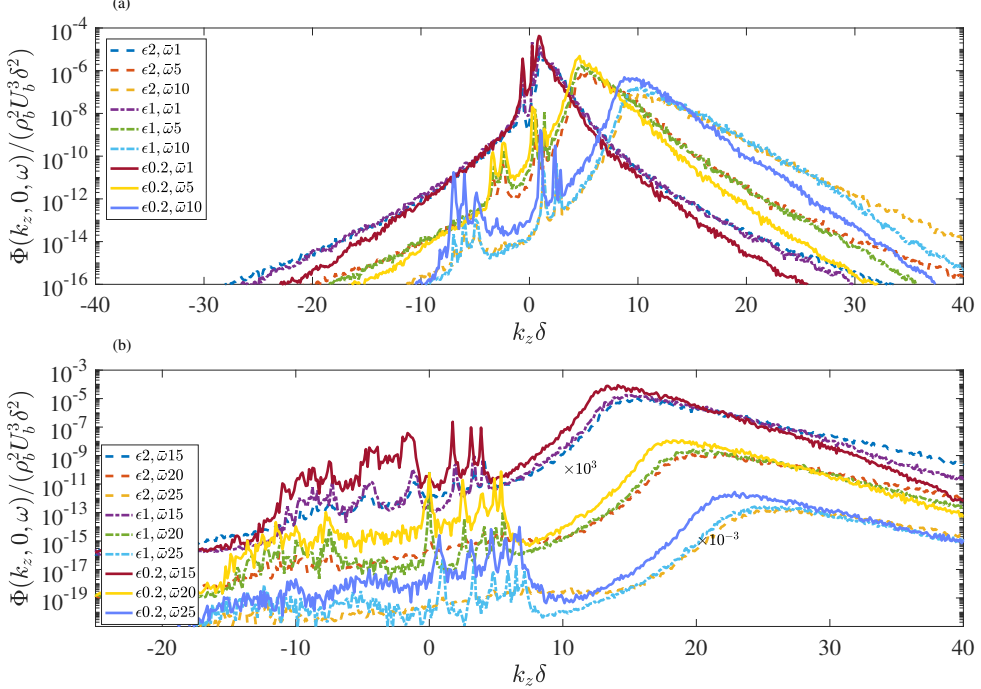


Figure 11: The non-dimensional 2D wavenumber-frequency spectra $\Phi(k_z, 0, \omega) / (\rho_b^2 U_b^3 \delta^2)$ over cylinders of various diameters; the spectral magnitudes at $\bar{\omega} = 15$ and $\bar{\omega} = 25$ are multiplied by 10^3 and 10^{-3} respectively for separation clarity.

approximately 10 dB higher than that on the outer wall. One therefore expects less energetic acoustic peaks for the radial order $n = 2$ on the outer wall.

As the frequency increases, figure 8(d-f) shows that more acoustic modes of higher radial orders become cut-on. To show these modes more closely, we choose a higher frequency of $k\delta = 10$ and plot the acoustic duct modes of radial orders 2 and 3 in figure 10. Again, high-order modes are cut-off. As the radial order increases, the acoustic pressure shows more zeros along the radial direction, while the streamwise wavenumber decreases. The latter is expected because of (4.6). Moreover, the difference in the pressure amplitude on the inner and outer walls appears larger as n increases. This suggests that the higher-order acoustic peaks in the WPF spectra are increasingly more pronounced on the inner wall than those on the outer wall. Note, however, although we can examine the behaviour of WPF on the outer walls, our primary concern in practice, and hence in this paper, is the WPF over the inner cylinder walls.

To compare the 2D wavenumber-frequency spectra over inner walls quantitatively, figure 11(a) shows $\Phi_{pp}(k_z, 0, \omega)$ against $k_z \delta$ at $\bar{\omega} = 1, 5$ and 10 . One can see that decreasing the diameter increases the spectral magnitude at low but decreases it at high wavenumbers. Different from figure 7(b), spectral peaks due to acoustic

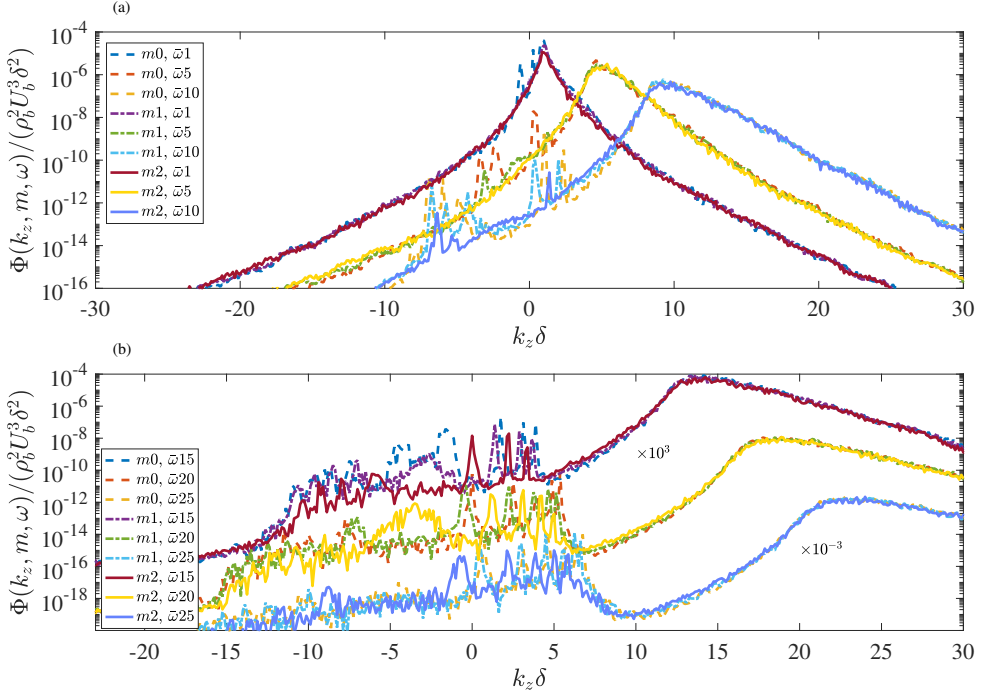


Figure 12: The non-dimensional 2D wavenumber-frequency spectra $\Phi(k_z, m, \omega) / (\rho_b^2 U_b^3 \delta^2)$ for azimuthal modes $m = 0, 1$ and 2 for $\epsilon = 0.2$; the spectral magnitudes at $\bar{\omega} = 15$ and $\bar{\omega} = 25$ are multiplied by 10^3 and 10^{-3} respectively for separation clarity.

duct modes can be found at all cylinder diameters. As shown in figure 8, these peak wavenumbers can be well predicted by (4.5). As the frequency increases, the low-wavenumber spectral augmentation appears stronger, as shown in figure 11(b). Note that when $\bar{\omega} \geq 20$, the low-wavenumber spectral magnitude at $\epsilon = 2$ is broadly elevated without apparent peaks, in accordance with Liu *et al.* (2024). But the acoustic peaks continue to show up when $\epsilon = 1$ and 0.2 . In addition, the acoustic peaks become more clustered because more duct modes are cut-on, as shown straightforwardly in figure 8. Clearly, when all azimuthal modes are summed to obtain $\Phi(k_z, \omega)$, more spectral peaks will appear, as evidenced by figure 7.

To show the variation of the wavenumber-frequency spectra against azimuthal modes, figure 12 shows the spectra at various m for $\epsilon = 0.2$. When the frequency is low ($\bar{\omega} = 1$), one can see that only the spectra at $m = 0$ exhibit acoustic peaks, since high-order modes are effectively cut-off according to (4.5). The spectral magnitude outside the acoustic peaks remains roughly identical. As the frequency increases to 5 and 10, acoustic modes at $m = 1$ and $m = 2$ become respectively cut-on. As the frequency further increases, more acoustic modes are cut-on and appear in the spectra shown in figure 12(b). Note that the elevated magnitude in the supersonic region appears to exist for all m . Other than that, the spectra look similar elsewhere.

This suggests a possible necessity of including WPF of higher azimuthal orders in some flow noise applications.

5. Discussions

The low-wavenumber augmentation in spectral magnitude as ϵ reduces is of great concern in practical applications such as towed sonar arrays (Bull 1996). To understand why such augmentation occurs, we start from modelling the WPF generated by a homogeneous turbulent boundary layer over an infinitely long cylinder. Note that such a model is not strictly applicable to the present setup, where channel flows within concentric annular ducts are simulated instead of free boundary layers. Nevertheless, we expect the effects of curvature on the WPF in these two cases remains similar, particularly at low wavenumbers. Therefore, we attempt to discuss the low-wavenumber WPF augmentation via modelling the boundary layer case.

5.1. Modelling WPF based on the Lighthill acoustic analogy

Using Lighthill's acoustic analogy and the acoustic Green's function, the WPF spectrum beneath a homogeneous turbulent boundary layer over an infinitely long cylinder can be found analytically as (Dhanak 1988)

$$\tilde{p}(k_z, m, \omega) = \int T_{ij}(\mathbf{y}, \tau) \frac{\partial^2}{\partial y_i \partial y_j} \left(-\frac{1}{\alpha R} \frac{H_m^{(1)}(\alpha r)}{H_m^{(1)'}(\alpha R)} e^{ik_z y} e^{im\phi} e^{-i\omega\tau} \right) d^3\mathbf{y} d\tau, \quad (5.1)$$

where T_{ij} ($i, j = 1, 2, 3$) is the Cartesian Lighthill's stress tensor, $\alpha = \sqrt{\omega^2/c_0^2 - k_z^2}$, $H_m^{(1)}(z)$ is the m th-order Hankel function of the first kind. The spatial integration in (5.1) is performed within the entire boundary layer over the cylinder. The 0th-order mode is of particular relevance, and in cylindrical coordinates shown in figure 2 it reduces to

$$\int_R^{R+\delta} \left[\frac{-\alpha H_0^{(1)''}(\alpha r)}{H_0^{(1)'}(\alpha R)} \tilde{T}_{rr} - \frac{H_0^{(1)''}(\alpha r)}{H_0^{(1)'}(\alpha R)} \left(\frac{\tilde{T}_{\theta\theta}}{r} + 2ik_z \tilde{T}_{rz} \right) + \frac{k_z^2 H_0^{(1)}(\alpha r)}{\alpha H_0^{(1)'}(\alpha R)} \tilde{T}_{zz} \right] \frac{r}{R} dr, \quad (5.2)$$

where the integral along the radial direction is from the cylinder radius R to the edge of the boundary layer $R + \delta$, while \tilde{T}_{ij} is the Fourier transform of Lighthill's stress tensor given by

$$\tilde{T}_{ij}(r, k_z, 0, \omega) = \iint T_{ij}(r, z, \theta, \omega) e^{ik_z z} e^{-i\omega\tau} dz d\theta d\tau, \quad (5.3)$$

where the subscripts i and j take the value of r , θ and z in the cylindrical coordinates. Equation (5.2) shows that the 0th-order WPF are only generated by the stress terms \tilde{T}_{rr} , $\tilde{T}_{\theta\theta}$, \tilde{T}_{rz} and \tilde{T}_{zz} within the boundary layer and are independent of $\tilde{T}_{\theta r}$ and $\tilde{T}_{z\theta}$. The latter two components are also expected to be small (see, for example, Appendix A for more details).

In the vicinity of the sonic peak $k_z = \omega/c_0$, the last term in (5.2) is singular, but

integrable. In practice, the height of these sonic peaks is regularised by the finite size and mean-flow refraction effects of the boundary layer (Bull 1996), details of which are not discussed here (note that in the channel flow case, more spectral peaks are expected apart from the sonic peak because of the presence of multiple cut-on duct modes). In most applications where the low-wavenumber components are of particular concern, one often has $k_z r \ll 1$ (r takes the value between R and $R + \delta$). In such cases, the last two terms of the right-hand side of (5.2) can be neglected except near the sonic singularity.

When the cylinder radius and boundary layer thickness are compact ($kR \ll 1$ and $k\delta \ll 1$, e.g. at low frequencies such as those in towed sonar arrays), (5.2) can be approximated using the small-argument expansion of the Hankel functions (Crighton *et al.* 1992) as

$$\tilde{p}(k_z, 0, \omega) \approx \int_0^1 \frac{\tilde{T}_{rr} - \tilde{T}_{\theta\theta}}{\epsilon + h} dh, \quad (5.4)$$

where $h \equiv y/\delta$ represents the non-dimensionalised radial distance measured from the inner cylinder wall and therefore takes the value from 0 to 1. On the other hand, when the cylinder radius is sufficiently non-compact (e.g. at sufficiently high frequencies), i.e. $kR \gg 1$, the Hankel functions can be expanded using their asymptotic form and (5.2) at low wavenumbers can be approximated as

$$\tilde{p}(k_z, 0, \omega) \approx \int_0^1 \sqrt{1 + \frac{h}{\epsilon}} \alpha \delta e^{i\alpha\delta h} e^{-i\frac{\pi}{2}} \tilde{T}_{rr} - \frac{1}{\sqrt{\epsilon(\epsilon + h)}} e^{i\alpha\delta h} \tilde{T}_{\theta\theta} dh. \quad (5.5)$$

Assuming that the distributions of Lighthill's stress tensors \tilde{T}_{rr} and $\tilde{T}_{\theta\theta}$ between the lower ($h = 0$) and upper walls ($h = 2$) do not change significantly as R varies, (5.4) and (5.5) show that the 0th-order spectrum at small k_z would increase when the radius of the inner cylinder reduces. This complies with the low-wavenumber increase of $\Phi(k_z, 0, \omega)$ observed at both low and high frequencies in figure 11. Note that the ϵ terms in equations (5.4) and (5.5) result from the asymptotic approximation of Hankel functions rather than from the Lighthill's stress. This suggests that the low-wavenumber increase is a "geometric" effect connected with the Green's function.

In particular, the appearance of $1/\sqrt{\epsilon(\epsilon + h)}$ in (5.5) as opposed to $1/(\epsilon + h)$ in (5.4) suggests that the amplification at high frequencies may be more pronounced than that at low frequencies. There exists indeed such a tendency in figure 11 as the frequency increases. Note that only radial and azimuthal velocity disturbances appear important. Moreover, both (5.4) and (5.5) suggest that as the curvature increases, disturbances close to the wall are increasingly more important in generating low-wavenumber components of the WPF spectrum. This complies with the fact that the convective velocity at a fixed $\omega\delta/u_\tau$ decreases as R reduces. This signals a potential for low-wavenumber WPF control using near-wall treatment on thin cylinders.

5.2. Comparison with DNS

In the derivation reaching (5.4) and (5.5), the assumption that the Lighthill stress tensors \tilde{T}_{rr} and $\tilde{T}_{\theta\theta}$ between the cylinder wall ($h = 0$) and outer edge of the boundary layer ($h = 1$) do not change significantly as R varies is important. To examine to what extent this assumption remains valid, we first show the wavenumber-frequency spectra of the two stress components, i.e. $\Psi_{rr}(r, k_z, 0, \omega)$ and $\Psi_{\theta\theta}(r, k_z, 0, \omega)$, along the wall-normal direction at a fixed frequency ω and wavenumber k_z . Note that the wavenumber-frequency spectra $\Psi_{rr} \propto |\tilde{T}_{rr}|^2$ while $\Psi_{\theta\theta} \propto |\tilde{T}_{\theta\theta}|^2$, therefore, $\sqrt{\Psi_{rr}}$ and $\sqrt{\Psi_{\theta\theta}}$ are shown in figures 13 to 16.

As mentioned above, we focus on the low-wavenumber region, where $k_z r \ll 1$ (r takes the value between R to $R + \delta$). However, the streamwise wavenumber resolution of the present simulation is only around $k_z \delta \approx 0.125$. This implies that the minimum non-zero wavenumber that can be resolved corresponds to a value of $k_z r$ up to 0.6. Therefore, we only show $\sqrt{\Psi_{rr}}$ and $\sqrt{\Psi_{\theta\theta}}$ at $k_z \delta = 0$ in this paper. Nevertheless, doing this does not reduce much generality, because the wavenumber-frequency spectrum has a well-known wavenumber-white behaviour (Bull 1996) near $k_z \delta = 0$, i.e. $\Phi(k_z, m, \omega)$ obtains a nearly constant value in the low-wavenumber range centring around $k_z \delta = 0$.

Note that the asymptotic form of (5.4) requires the cylinder to be acoustically compact, i.e. $kR \ll 1$ and $k\delta \ll 1$. This corresponds to a low-frequency range, which we can properly resolve with a frequency resolution of $\omega\delta/U_b \approx 0.165$ ($k\delta \approx 0.01$). However, the asymptotic form of (5.5) requires acoustic non-compactness, i.e. $kR \gg 1$. This implies a considerably high frequency range. To put this into perspective, for $\epsilon = 0.2$, a moderate number $kR = 2$ corresponds to a frequency of $\omega\delta/U_b = 157$. Resolving such a frequency needs a very high sampling rate of the flow snapshots, and in practice storing this tremendous amount of data is prohibitively expensive. More importantly, in practical applications, it is the low frequencies that are of our primary concern. As such, in the following, we focus on examining the distribution of $\sqrt{\Psi_{rr}}$ and $\sqrt{\Psi_{\theta\theta}}$ at low frequencies where the cylinder is acoustically compact.

Figure 13 shows the amplitude spectra of $\tilde{T}_{rr}(r, 0, 0, 0)$ and $\tilde{T}_{\theta\theta}(r, 0, 0, 0)$. These are the steady and homogeneous components of the Lighthill stress tensors and should be more properly interpreted as propagation effects rather than as a source in the acoustic analogy framework. Nevertheless, we see that as curvature increases, the two steady stress components generally decrease in amplitude. However, they do not differ from each other by orders of magnitude. In terms of decibels the difference in their amplitudes is limited by 3 dB.

The distribution at $k_z \delta = 0$ and $\omega\delta/U_b \approx 0.165$, as demonstrated in figure 14, shows a similar story. However, it is worth noting that the amplitude becomes much smaller than that at $\omega\delta/U_b = 0$. Such a trend further continues as frequency increases, as shown in figures 15 and 16, where the non-dimensional frequency

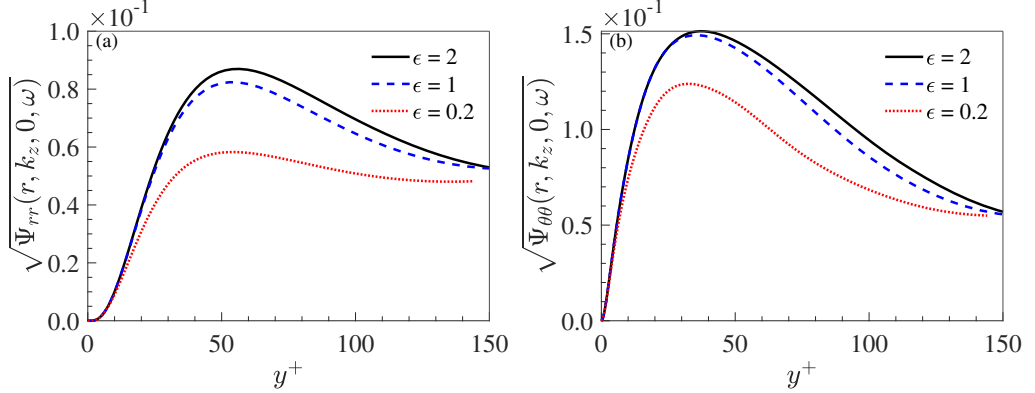


Figure 13: Wall normal distribution of the Lighthill stress components (a) \tilde{T}_{rr} and (b) $\tilde{T}_{\theta\theta}$ over inner cylinder surface at $k_z\delta = 0$ and $\omega\delta/U_b = 0$.

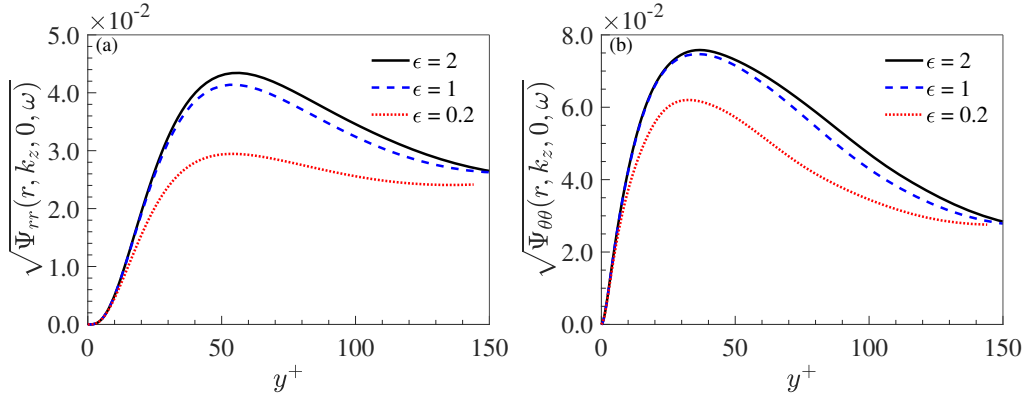


Figure 14: Wall normal distribution of the Lighthill stress components (a) \tilde{T}_{rr} and (b) $\tilde{T}_{\theta\theta}$ over inner cylinder surface at $k_z\delta = 0$ and $\omega\delta/U_b \approx 0.165$.

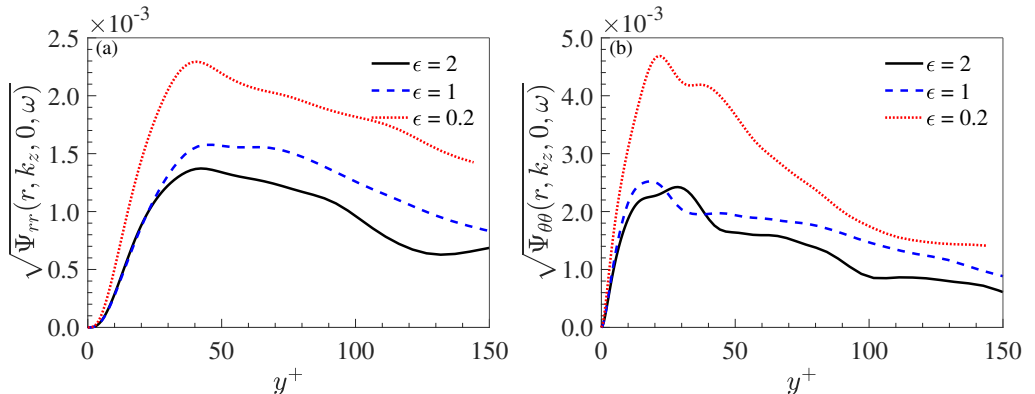


Figure 15: Wall normal distribution of the Lighthill stress components (a) \tilde{T}_{rr} and (b) $\tilde{T}_{\theta\theta}$ over inner cylinder surface at $k_z\delta = 0$ and $\omega\delta/U_b \approx 0.33$.

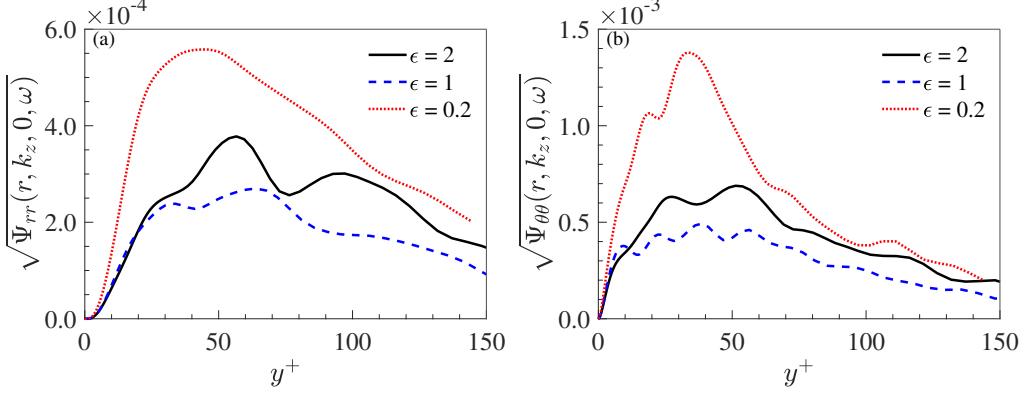


Figure 16: Wall normal distribution of the Lighthill stress components (a) \tilde{T}_{rr} and (b) $\tilde{T}_{\theta\theta}$ over inner cylinder surface at $k_z\delta = 0$ and $\omega\delta/U_b \approx 1.16$.

$\omega\delta/U_b \approx 0.33$ and 1.16 , respectively. This is consistent with the fact the low-wavenumber WPF decreases quickly as frequency increases. Unlike figures 13 and 14, figures 15 and 16 show that the amplitudes of $\tilde{T}_{\theta\theta}$ and \tilde{T}_{rr} largely increase as the curvature increases. However, the difference is not significant. Distributions of these two stress components at even higher frequencies are shown in Appendix B. It is worth noting that as frequency increases, the Lighthill stress components appear to converge increasingly less satisfactorily.

We can now calculate both \tilde{T}_{rr} and $\tilde{T}_{\theta\theta}$ and predict the wavenumber-frequency spectra of the WPF using (5.4). Note that the model developed in this section is for the WPF beneath a homogeneous turbulent boundary layer; therefore, it is not strictly applicable to the present channel flows. Nevertheless, we can still compare the model prediction with the simulation results, hoping to capture the important trend instead of seeking an exact agreement.

Results are shown in figure 17, where the predicted WPF wavenumber-frequency spectra $\Phi(k_z, m, \omega)$ for the axisymmetric ($m = 0$) mode at low frequencies are compared with DNS results. Again, since we are primarily interested in the low-wavenumber where the WPF has a “wavenumber white” behaviour near $k_z\delta = 0$, we show the spectrum $\Phi(0, 0, \omega)$ as a function of ω . The predicted spectra are obtained from (5.4) using \tilde{T}_{rr} and $\tilde{T}_{\theta\theta}$ examined in figures 13 to 16. From figure 17, we can see that spectral augmentation as ϵ decreases is well-predicted from the asymptotic equation. As ϵ decreases from 2 to 0.2, the amplitude of the DNS WPF spectra increases by almost two orders of magnitude. This trend is well captured in the prediction. Considering that \tilde{T}_{rr} and $\tilde{T}_{\theta\theta}$ do not change significantly as ϵ varies, this augmentation is indeed primarily contributed by the $\epsilon + h$ term in (5.4).

In addition, outside the acoustic peaks, the predicted spectra follow the DNS results closely. The agreement is slightly better for $\epsilon = 2$ and $\epsilon = 1$, while the spectrum of $\epsilon = 0.2$ is slightly over-predicted. Note that decreasing the upper

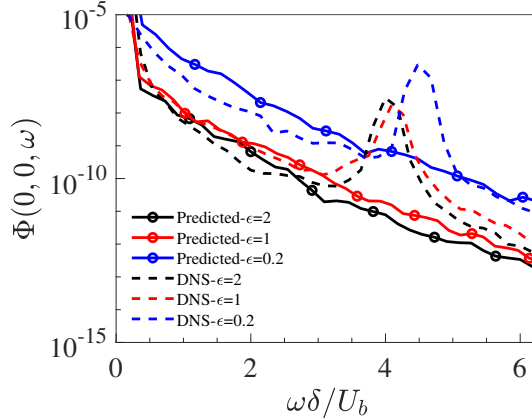


Figure 17: Comparison of the WPF wavenumber frequency spectrum $\Phi(0,0,\omega)$ between the asymptotic prediction and DNS results.

interval limit of the integral in (5.4) slightly reduces the predicted Φ amplitude significantly for $\epsilon = 2$ and 1, but the variation is negligible for $\epsilon = 0.2$. This is a direct demonstration that disturbances closer to the wall are increasingly important in generating WPF as the inner cylinder becomes thinner. Considering that the model does differ from the channel flow setup, such an agreement is sufficient to show the validity of (5.4).

6. Conclusion and future work

Compressible DNS simulations within concentric annular ducts are performed in this paper to study the effects of curvature on the WPF characteristics over cylindrical walls. The inner cylinder radius R ranges from 0.2δ , δ , 2δ to ∞ . The simulations are validated against previous results in the literature, and the effects of curvature on the flow statistics are discussed. It is found that, as the curvature increases, the three normal Reynolds stress components, together with $\langle u_r' u_z' \rangle$, over the inner cylinder wall decrease and peak slightly closer to the wall. However, the flows over the outer cylinder wall show an opposite behaviour.

Regarding the WPF, results show that, as R decreases, the magnitude of the one-point PSD of the WPF decreases at intermediate but increases at high frequencies. The magnitude of the 1D streamwise wavenumber-frequency spectrum decreases at high wavenumbers. Moreover, as R reduces to 0.2δ , the spectra start to show acoustic peaks at low wavenumbers, whose strengths become increasingly strong at higher frequencies. These acoustic peaks represent acoustic duct modes within the concentric annular channel. An examination of these modes shows that the plane wave mode (1st-order radial mode) does not discriminate between the inner and outer walls in terms of pressure amplitude, however, modes of higher radial orders are increasingly more energetic on the inner walls.

The 0th-order 2D wavenumber-frequency spectrum is of great importance in practical applications. DNS shows that reducing R decreases the high-wavenumber but increases the low-wavenumber components. In particular, the low-wavenumber increase appears stronger at high frequencies. Analytical modelling based on the Lighthill acoustic analogy shows that this arises primarily from the “geometric” effects connected with the Green’s function. Asymptotic prediction of this model agrees well with the DNS results at low frequencies. The 0th-order low-wavenumber WPF is generated mainly by azimuthal and radial disturbances. Moreover, disturbances close to the wall play an increasingly important role in generating WPF as the curvature increases. This is important as it suggests a possibility of low-wavenumber WPF control using wall treatments. At $R = 0.2\delta$, 2D wavenumber-frequency spectra of higher azimuthal orders are virtually identical to the 0th-order except nearby acoustic ridges.

The present work mainly focuses on the effects of curvature on the WPF characteristics. The effects of Mach number are examined in [Liu et al. \(2024\)](#) for rectangular channels. It is, however, worth studying how these effects change in the annular channel. The difference in WPF between channel flows and free boundary layers also warrants investigations. These form part of our future work.

Acknowledgements. The authors wish to thank Prof. Richard D. Sandberg for the license of using the code HiPSTAR, and Prof. Meng Wang for inspiring discussions on compressible DNS simulations.

Funding. The authors wish to gratefully acknowledge the National Natural Science Foundation of China (NSFC) under grant numbers 12472263, U25700222, 92152202, 12432010, 12588201 and 12572247.

Declaration of interests. The authors report no conflict of interest.

Appendix A. Distribution of other Reynolds stress components

The wall-normal distribution of the other two Reynolds stress components, i.e. $\langle u_z' u_\theta'^+ \rangle$ and $\langle u_r' u_\theta'^+ \rangle$ over the inner and outer cylinder walls are shown in figure 18. Among them, figures 18(a) and (b) show the two components over the inner wall. First of all, as expected, both $\langle u_r' u_\theta'^+ \rangle$ and $\langle u_z' u_\theta'^+ \rangle$ are two orders of magnitude smaller than other Reynolds stress components, while the former appears larger than the latter. In addition, the plane channel flow appears to have the largest value. The wall-normal distributions over the outer cylinder wall, as shown in figures 18(c) and (d), are generally similar. It is also worth mentioning that neither component contributes to the 0th-order WPF wavenumber-frequency spectra, as shown in section 5.

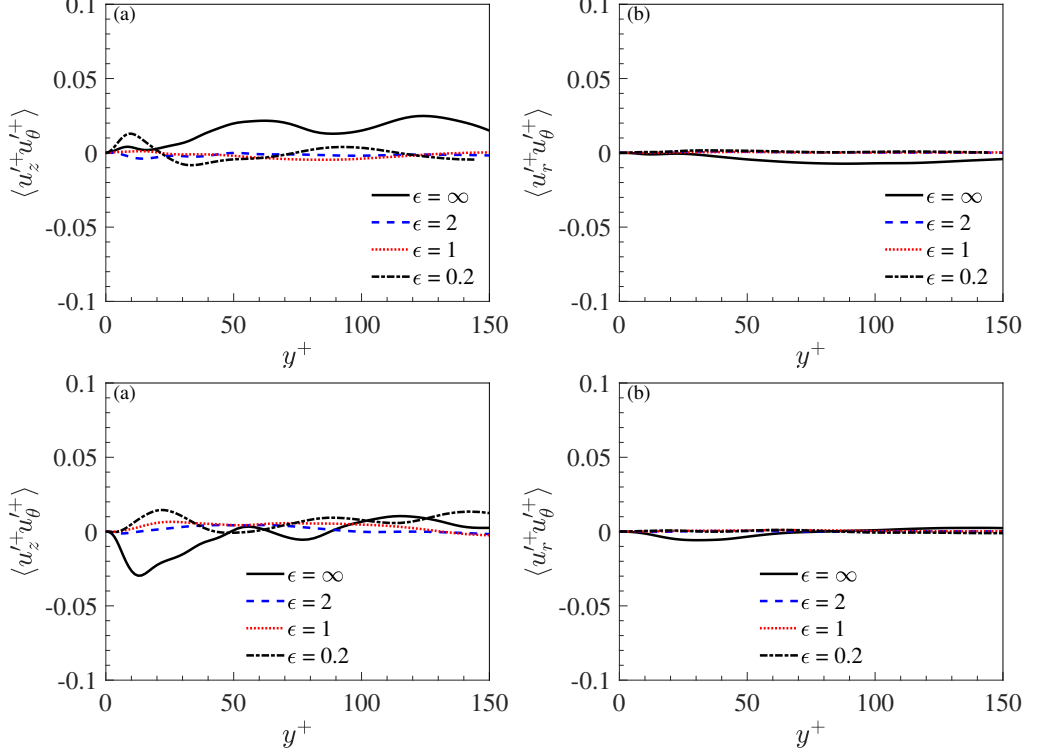


Figure 18: Wall normal distribution of the Reynolds stresses of (a) $\langle u_z' u_\theta' \rangle$ and (b) $\langle u_r' u_\theta' \rangle$ over inner cylinder wall and (c) $\langle u_z' u_\theta' \rangle$ and (d) $\langle u_r' u_\theta' \rangle$ over outer cylinder wall.

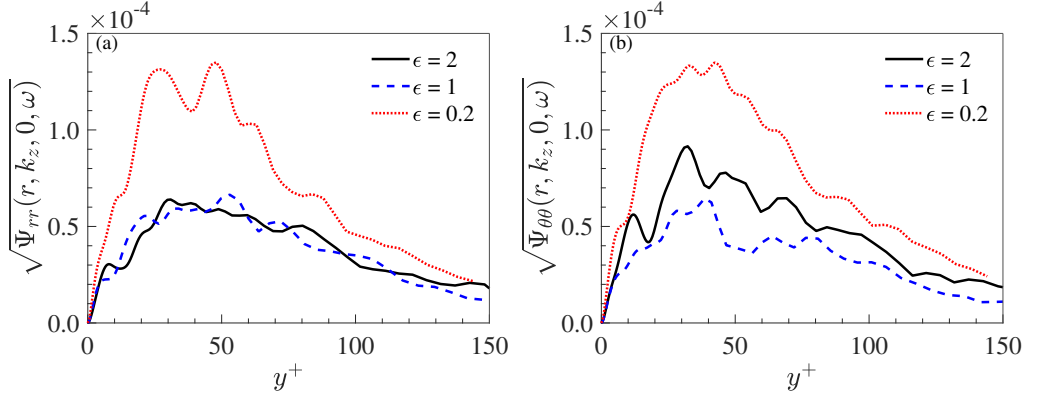


Figure 19: Wall normal distribution of the Lighthill stress components (a) \tilde{T}_{rr} and (b) $\tilde{T}_{\theta\theta}$ over inner cylinder surface at $k_z \delta = 0$ and $\omega \delta / U_b = \pi$.

Appendix B. Distribution of other Lighthill stress components

To further examine the assumption that $\tilde{T}_{\theta\theta}$ and \tilde{T}_{rr} do not change significantly as curvature varies, we also show the distribution of them at $\omega \delta / U_b = \pi$ and 2π in figure 19 and 20, respectively. These correspond to $k\delta$ values of 0.2 and 0.4,

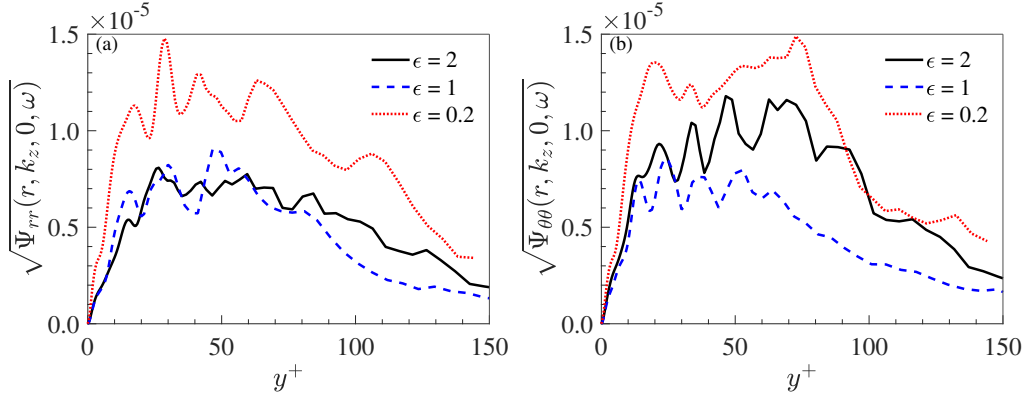


Figure 20: Wall normal distribution of the Lighthill stress components (a) \tilde{T}_{rr} and (b) $\tilde{T}_{\theta\theta}$ over inner cylinder surface at $k_z\delta = 0$ and $\omega\delta/U_b = 2\pi$.

respectively. The case of $\omega\delta/U_b = \pi$ shown in figure 19 is similar to that in figure 16, where the amplitudes of \tilde{T}_{rr} and $\tilde{T}_{\theta\theta}$ grows larger when $\epsilon = 0.2$. However, the difference is not significant. Examining these distributions at $\omega\delta/U_b = 2\pi$ in figure 20, we note first that the amplitudes of both components have decayed significantly to 10^{-5} . In addition, one can see that as curvature increases, both $\tilde{T}_{\theta\theta}$ and \tilde{T}_{rr} increase only slightly. The difference between them is small. From figures 13 to 20, it is clear that these Lighthill stress components indeed do not differ significantly at the low frequencies.

REFERENCES

BAGHERI, E. & WANG, B.-C. 2020 Effects of radius ratio on turbulent concentric annular pipe flow and structures. *International Journal of Heat and Fluid Flow* **86**, 108725.

BLAKE, W. K. 1970 Turbulent boundary-layer wall-pressure fluctuations on smooth and rough walls. *Journal of Fluid Mechanics* **44** (4), 637–660.

BOGEY, CHRISTOPHE & BAILLY, CHRISTOPHE 2004 A family of low dispersive and low dissipative explicit schemes for flow and noise computations. *Journal of Computational physics* **194** (1), 194–214.

BULL, M. K. 1967 Wall pressure fluctuations associated with subsonic turbulent boundary layer flow. *Journal of Fluid Mechanics* **28**, 719–7544.

BULL, M. K. 1996 Wall-pressure fluctuations beneath turbulent boundary layers: some reflections on forty years of research. *Journal of Sound and Vibration* **190**, 299–315.

COHEN, E. & GLOERFELT, X. 2018 Influence of pressure gradients on wall pressure beneath a turbulent boundary layer. *Journal of Fluid Mechanics* **838**, 715–758.

CORCOS, G. M. 1963 Resolution of pressure in turbulence. *Journal of Acoustical Society of America* **35**, 192–199.

CRIGHTON, DAVID GEORGE, DOWLING, ANN P, FFOWCS-WILLIAMS, J. E., HECKL, MANFRED, LEPPINGTON, FG & BARTRAM, JAMES F 1992 Modern methods in analytical acoustics lecture notes Publisher: Acoustical Society of America.

DEUSE, MATHIEU & SANDBERG, RICHARD D. 2020 Different noise generation mechanisms of

a controlled diffusion aerofoil and their dependence on mach number. *Journal of Sound and Vibration* **476**, 115317.

DHANAK, M. R. 1988 Turbulent boundary layer on circular cylinder: the low-wavenumber surface pressure spectrum due to a low-mach number flow. *Journal of Fluid Mechanics* **191**, 443–464.

DOWLING, A.P. 1998 Underwater flow noise. *Theoretical and Computational Fluid Dynamics* **10** (1), 135–153.

FFOWCS-WILLIAMS, J. E. 1965 Surface-pressure fluctuations induced by boundary-layer flow at finite Mach number. *Journal of Fluid Mechanics* **22** (3), 507–519, publisher: Cambridge University Press.

GLOERFELT, X. & BERLAND, J. 2013 Turbulent boundary-layer noise: direct radiation at mach number 0.5. *Journal of Fluid Mechanics* **723**, 318–351.

HARRISON, M. 1958 Pressure fluctuations on the wall adjacent to a turbulent boundary layer. Report No. 1260. U.S. Navy David Taylor Model Basin.

HOWE, M. S. 1987 On the structure of the turbulent boundary-layer wall pressure spectrum in the vicinity of the acoustic wavenumber. *Proceedings of the Royal Society, London A* **412**, 389–401.

KENNEDY, C. A., CARPENTER, M. H. & LEWIS, R. M. 2000 Low-storage, explicit Runge–Kutta schemes for the compressible Navier–Stokes equations. *Appl. Numer. Math.* **35** (3), 177–219.

KENNEDY, CHRISTOPHER A. & GRUBER, ANDREA 2008 Reduced aliasing formulations of the convective terms within the navier–stokes equations for a compressible fluid. *Journal of Computational Physics* **227** (3), 1676–1700.

KRAICHNAN, ROBERT H 1956 Pressure fluctuations in turbulent flow over a flat plate. *The Journal of the Acoustical Society of America* **28** (3), 378–390, publisher: Acoustical Society of America.

LIU, Y., WANG, K. & WANG, M. 2024 Subconvective wall-pressure fluctuations in low-mach-number turbulent channel flow. *Journal of Fluid Mechanics* **984** (R2), 1–13.

NEVES, J. C. & MOIN, P. 1994a Effects of convex transverse curvature on wall-bounded turbulence. part 1. velocity and vorticity. *Journal of Fluid Mechanics* **272**, 349–381.

NEVES, J. C. & MOIN, P. 1994b Effects of convex transverse curvature on wall-bounded turbulence. part 2. the pressure fluctuations. *Journal of Fluid Mechanics* **272**, 383–406.

POPE, S. B. 2000 *Turbulent Flows*. Cambridge University Press.

SANDBERG, R. D., MICHELASSI, V., PICHLER, R., CHEN, L. & JOHNSTONE, R. 2015 Compressible direct numerical simulation of low-pressure turbines—Part I: Methodology. *J. Turbomach.* **137** (5), 051011.

WHITE, F. M. 1991 *Viscous fluid flow*. McGraw-Hill, New York.

WILLMARTH, W. W. 1956 Wall pressure fluctuations in a turbulent boundary layer. *Journal of Acoustical Society of America* **28**, 1048–1053.

WILLMARTH, W. W. 1958 Space-time correlations of the fluctuating wall pressure in a turbulent boundary layer. *Journal of Aerospace Science* **25**, 335–336.

WILLMARTH, W. W. 1975 Pressure fluctuations beneath turbulent boundary layers. *Annual Review of Fluid Mechanics* **7**, 13–36.

WILLMARTH, W. W., WINKEL, R. E., SHARMA, L. K. & BOGAR, T. J. 1976 Axially symmetric turbulent boundary layers on cylinders: Mean velocity profiles and wall pressure fluctuations. *Journal of Fluid Mechanics* **76**, 35–64.

WILLMARTH, W. W. & YANG, C. S. 1970 Wall pressure fluctuations beneath turbulent boundary layer on a flat plate and a cylinder. *Journal of Fluid Mechanics* **41**, 47–80.